

# Size-Tunable Ni–Cu Core–Shell Nanoparticles—Structure, Composition, and Catalytic Activity for the Reverse Water–Gas Shift Reaction

Maria Heilmann, Carsten Prinz, Ralf Bienert, Robert Wendt, Benny Kunkel, Jörg Radnik, Armin Hoell, Sebastian Wohlrab, Ana Guilherme Buzanich, and Franziska Emmerling\*

A facile and efficient methodology is described for the solvothermal synthesis of size-tunable, stable, and uniform NiCu core–shell nanoparticles (NPs) for application in catalysis. The diameter of the NPs is tuned in a range from 6 nm to 30 nm and to adjust the Ni:Cu ratio from 30:1 to 1:1. Furthermore, the influence of different reaction parameters on the final NPs is studied. The NPs are structurally characterized by a method combination of transmission electron microscopy, anomalous small-angle X-ray scattering, X-ray absorption fine structure, and X-ray photoelectron spectroscopy. Using these analytical methods, it is possible to elucidate a core–shell–shell structure of all particles and their chemical composition. In all cases, a depletion from the core to the shell is observed, with the core consisting of NiCu alloy, surrounded by an inner Ni-rich shell and an outer NiO shell. The SiO<sub>2</sub>-supported NiCu core–shell NPs show pronounced selectivity of >99% for CO in the catalytic reduction of CO<sub>2</sub> to CO using hydrogen as reactant (reverse water–gas shift reaction) independent of size and Ni:Cu ratio.

reaction.<sup>[8]</sup> Monometallic nickel (Ni) and copper (Cu) NPs play important roles for the catalysis of the alkaline hydrogen evolution reaction,<sup>[9]</sup> antibacterial applications,<sup>[10]</sup> the oxygen reduction reaction,<sup>[11]</sup> the Sabatier reaction,<sup>[12]</sup> and the RWGS reaction.<sup>[13–16]</sup>

Ni mono- and bi-metallic NPs can be prepared by different bottom-up and top-down approaches such as thermal decomposition,<sup>[17]</sup> laser ablation,<sup>[18]</sup> atomic layer deposition,<sup>[19]</sup> microwave-assisted synthesis,<sup>[20]</sup> sol-gel technique,<sup>[21]</sup> colloidal synthesis,<sup>[22]</sup> and thermal reduction.<sup>[23]</sup> A common synthesis for monometallic Ni NPs is the thermal reduction of metal precursors at elevated temperatures around 220 °C, often performed with oleylamine as reducing agent and trioctylphosphine as stabilizer.<sup>[24,25]</sup> The reaction is well studied,


which allows tuning of NP size and shape by varying the reaction parameters such as the amount of reducing and stabilizing agent.<sup>[26,27]</sup> The drawback of this synthesis route is the need for inert conditions, which is often realized by standard air-free conditions using inert gas or vacuum in space- and equipment-consuming Schlenk conditions. An adapted facile and straightforward synthesis method employed by our group can be used to reduce the expenditure.<sup>[25]</sup>

## 1. Introduction

Nanoparticles (NPs) are of great interest due to their unique properties and the variety of applications in, for example, catalysts, sensor materials, and analytical assays.<sup>[1–3]</sup> In particular, metal NPs are relevant for drug delivery,<sup>[4]</sup> biosensing,<sup>[5]</sup> and as catalysts for the hydrogen evolution reaction,<sup>[6]</sup> the acidic oxygen evolution reaction,<sup>[7]</sup> and the reverse water–gas shift (RWGS)

M. Heilmann, C. Prinz, R. Bienert, A. Guilherme Buzanich, F. Emmerling  
Structure Analysis  
Federal Institute for Materials Research and Testing (BAM)  
Richard-Willstätter-Str. 11, D-12489 Berlin, Germany  
E-mail: franziska.emmerling@bam.de

J. Radnik  
Surface Analysis and Interfacial Chemistry  
Federal Institute for Materials Research and Testing (BAM)  
Richard-Willstätter-Str. 11, D-12489 Berlin, Germany

 The ORCID identification number(s) for the author(s) of this article can be found under <https://doi.org/10.1002/adem.202101308>.

© 2022 The Authors. Advanced Engineering Materials published by Wiley-VCH GmbH. This is an open access article under the terms of the Creative Commons Attribution License, which permits use, distribution and reproduction in any medium, provided the original work is properly cited.

DOI: 10.1002/adem.202101308

M. Heilmann, F. Emmerling  
Department of Chemistry  
Humboldt-Universität zu Berlin  
Brook-Taylor-Str. 2, D-12489 Berlin, Germany

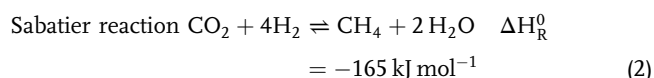
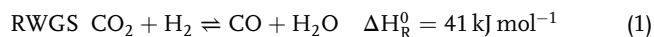
R. Wendt  
Solar Fuels  
Helmholtz-Zentrum Berlin für Materialien und Energie GmbH  
Hahn-Meitner-Platz 1, D-14109 Berlin, Germany

A. Hoell  
Structure and Dynamics of Energy Materials  
Helmholtz-Zentrum Berlin für Materialien und Energie GmbH  
Hahn-Meitner-Platz 1, D-14109 Berlin, Germany

B. Kunkel, S. Wohlrab  
Leibniz-Institut für Katalyse e.V.  
Albert-Einstein-Str. 29a, D-18059 Rostock, Germany

Bimetallic Ni NPs have been rarely produced via this thermal reduction pathway. Carenco et al. prepared core-shell NiCo NPs in a two-step synthesis route<sup>[28]</sup> and Guo et al. synthesized alloyed NiCu NPs with a polydispersity of around 30% by a co-reduction of nickel acetylacetonate and copper acetylacetonate with trioctylphosphine in oleylamine at temperatures around 230 °C.<sup>[29]</sup>

Ni and Cu are suitable catalyst materials for the conversion of carbon dioxide (CO<sub>2</sub>) to carbon monoxide (CO) with hydrogen (H<sub>2</sub>) under atmospheric pressure via the RWGS reaction (Equation (1)),<sup>[13]</sup> or to methane (CH<sub>4</sub>) via the Sabatier reaction (Equation (2))<sup>[12,30]</sup>



The first reaction, RWGS, is a promising approach to convert CO<sub>2</sub> to valuable chemicals and fuels, and it can close an energy-saving cycle in the power-to-syngas process.<sup>[31]</sup>

In addition to a suitable activity of the catalyst, the selectivity toward CO and not CH<sub>4</sub> must also be given. However, this has proved to be a problem in the past, especially with monometallic Ni catalysts, as the formation of methane is preferred above a certain particle size.<sup>[14,32,33]</sup>

Here, we present a straightforward and much more time- and space-saving synthesis strategy for NiCu NPs. The resulting NiCu NPs were investigated explicitly for their potential use in RWGS. In this study, we tested the influence of different syntheses parameters (amount of reducing agent and stabilizer) on the size of the final NPs.

For the understanding of nanomaterials, a thorough characterization is necessary, which can be achieved by combining different analytical methods such as imaging techniques (transmission electron microscopy [TEM]), chemical state analysis (X-ray absorption spectroscopy [XAS]), surface sensitive elemental composition analysis (X-ray photoelectron spectroscopy [XPS]), and element specific structural analysis (anomalous small-angle X-ray scattering [ASAXS]). The combination of these

techniques allows the identification of the inner structure of the final NiCu NPs.

The optimized NPs were then subjected to catalytic tests, revealing a pronounced selectivity for CO, independent of the particle size. Our study shows that a careful fine-tuning of particle properties opens a pathway to new catalysts.

## 2. Results and Discussion

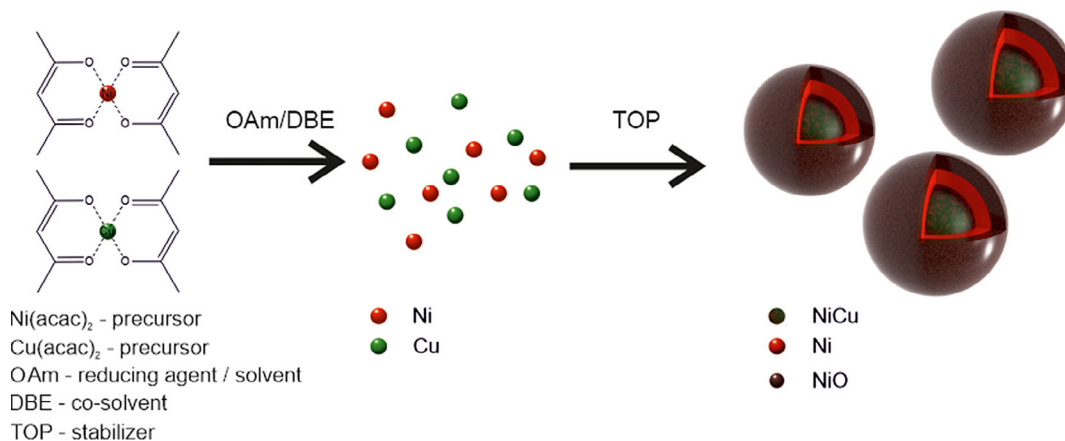
The typical synthesis procedure of the solvothermal reduction of Ni(acac)<sub>2</sub> and Cu(acac)<sub>2</sub> is shown in **Scheme 1**. In this process, Ni(acac)<sub>2</sub> and Cu(acac)<sub>2</sub> are dissolved in oleylamine (OAm) and dibenzyl ether (DBE), the complexes are reduced to metallic atoms by OAm, and they grow to metallic NPs, supported by the stabilizing agent trioctylphosphine (TOP), as previously indicated by An et al.<sup>[34]</sup>

### 2.1. Physical Characterization of Bimetallic NiCu NPs

Size-tunable synthesis of spherical bimetallic NiCu NPs is enabled by this synthesis route. Using 30 mmol L<sup>-1</sup> metal precursor, with an Ni:Cu ratio of 5:1, and 10 equivalents (eq) TOP in 5 mL OAm (90 eq) leads to 16 nm sized NiCu NPs.

SAXS analyses of the final NP dispersion resulted in a diameter of 16.8 nm with a distribution of 14% using a Weibull distribution<sup>[35]</sup> (see **Figure 1a**). TEM measurements shown in **Figure 1b,c** indicate the formation of spherical and nearly monodisperse NPs, which applies to the whole NP size range, as shown in **Figure S2c**, Supporting Information. The XRD pattern of the NP dispersion (black line in **Figure 1d**) exhibits reflections of crystalline Ni and Cu, indicating that the NPs contain crystalline domains. This finding of non-oxidized Ni and Cu in the XRD pattern is in accordance with Liu et al. and An et al.<sup>[34,36]</sup>

STEM energy dispersive X-ray spectroscopy (EDX) measurements of these particles indicate the formation of a core-shell structure with Cu in the center surrounded by an Ni layer as evident from the line scan of representative particles (**Figure 1e**) and in the element mapping (**Figure 1f**, more detailed in **Figure S2b**,



**Scheme 1.** Schematic representation of the NiCu NPs synthesis conditions using nickel(II) acetylacetonate (Ni(acac)<sub>2</sub>) and copper(II) acetylacetonate (Cu(acac)<sub>2</sub>) as precursors, oleylamine (OAm) as reducing agent and solvent, dibenzyl ether (DBE) as cosolvent, and trioctylphosphine (TOP) as stabilizer.

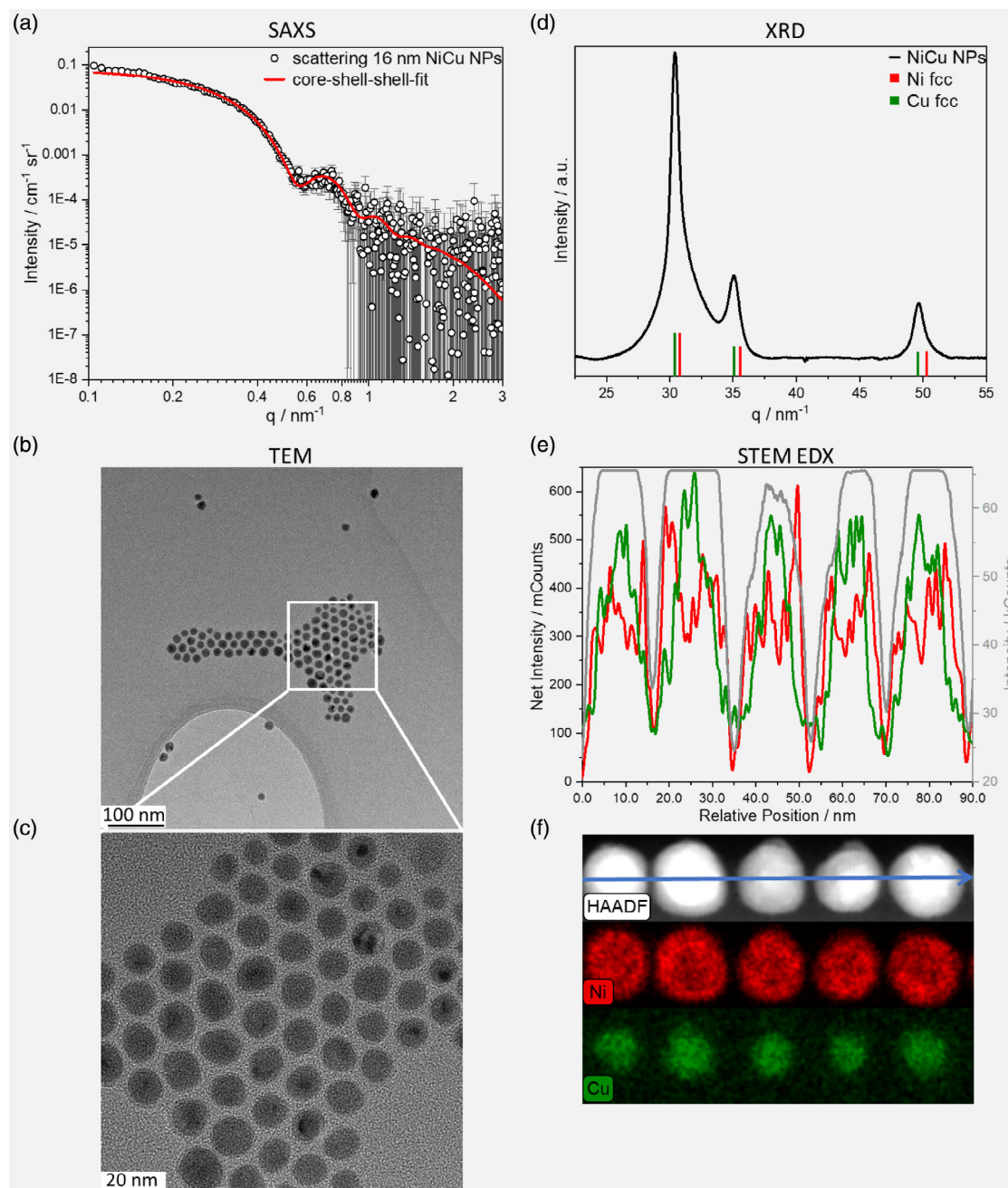


**Figure 1.** Characterization of bimetallic NPs a) SAXS curve of 16 nm NiCu NPs (black circles) fitted with a core-shell-shell model (red line); b) and c) TEM images of the final NiCu NPs showing nearly monodisperse spherical 16 nm particles; d) background-subtracted XRD pattern of 16 nm NiCu NPs compared with the database entries JCPDS database PDF 04-0850 for bulk Ni (black), COD 4 313 203 for bulk Cu (red), and COD 9 008 693 for bulk NiO (blue); e) Line scan of bimetallic NiCu NPs (16 nm) showing the intensity of the HAADF signal (grey, scale right) and the net intensities of Ni (red) and Cu (green, scale left); and f) STEM image with blue arrow indicating the line scan and EDX mappings of the elements Ni and Cu.

Supporting Information). The structure can be explained with the different standard potentials of Cu and Ni. The standard potential of Cu ( $E^0(\text{Cu}^{2+}/\text{Cu}) = 0.34 \text{ V}$ ) is higher than Ni ( $E^0(\text{Ni}^{2+}/\text{Ni}) = -0.23 \text{ V}$ ), which means that Cu is easier to reduce while Ni requires harsher conditions. Thus, Cu is reduced first, followed by Ni, leading to NiCu core-shell NPs. High-resolution TEM images of NiCu NPs with varying sizes are added in Figure S2a, Supporting Information. It can be seen that the

NPs consist of smaller crystalline domains, suggesting strong surface irregularities.

XANES and EXAFS measurements were conducted to investigate the oxidation state and local structure of Ni and Cu atoms in the NPs. The Ni and Cu K-edge XANES spectra of 16 nm NPs are shown in Figure 2a,b, respectively. The Ni XANES spectrum exhibits features of both metallic Ni and NiO. The shape of the absorption maximum (white line) resembles the one from NiO to

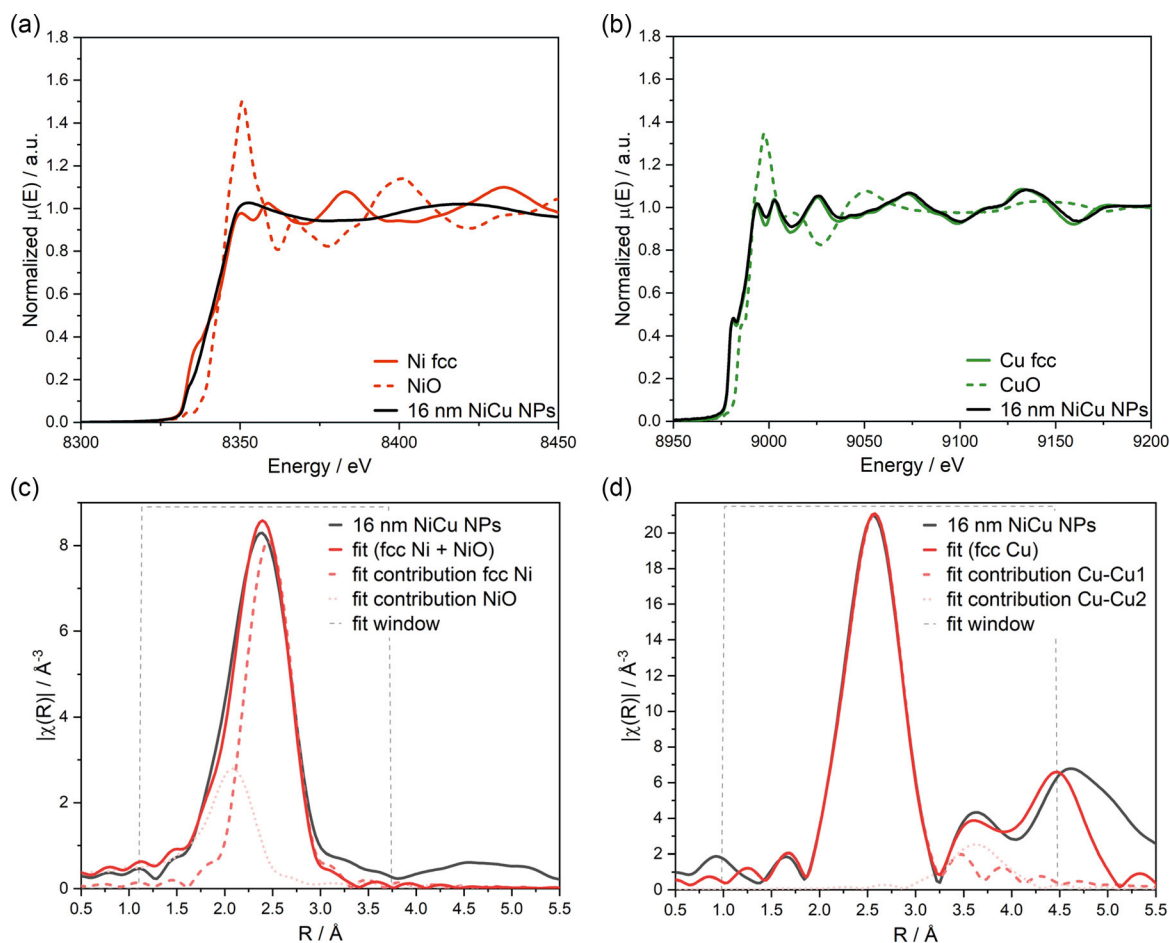


**Figure 2.** a) Normalized Ni K-edge XANES spectra of bimetallic 16 nm NiCu NPs (black), an Ni film (red solid), and NiO (red dotted); b) normalized Cu K-edge XANES spectra of bimetallic 16 nm NiCu NPs (black), a Cu film (green), and CuO (green dotted); c) magnitude of EXAFS oscillations ( $|\chi(R)|$ ) as a function of the interatomic distance  $R$  obtained by Fourier transformation of NiCu NPs (black) and fcc Ni bulk and NiO fit (red); d) magnitude EXAFS oscillations ( $|\chi(R)|$ ) as a function of the interatomic distance  $R$  obtained by Fourier transformation of NiCu NPs (black) and fcc Cu bulk fit (red).

**Table 1.** Comparison of the fitted EXAFS data of 16 nm NiCu NPs with the structural parameters of bulk Ni(fcc), NiO (RMSE = 0.09 Å, red.  $\chi^2 = 2118$ ), and bulk Cu(fcc) (RMSE = 0.03 Å, red.  $\chi^2 = 367$ ).

|                            | Coordination Number |              | Distance $R$ [Å]   |                  |                     |
|----------------------------|---------------------|--------------|--------------------|------------------|---------------------|
|                            | bulk                | NiCu NPs     | $R_{\text{model}}$ | $R_{\text{fit}}$ | $R^2_{\text{diff}}$ |
| Ni <sub>fcc</sub> (Ni–Ni)  | 12                  | 5.31 ± 0.72  | 2.49               | 2.48             | 0.001               |
| NiO (Ni–O)                 | 6                   | 3.37 ± 0.31  | 2.09               | 2.21             | 0.016               |
| Cu <sub>fcc</sub> (Cu–Cu1) | 12                  | 12.21 ± 1.25 | 2.56               | 2.53             | 0.001               |
| Cu <sub>fcc</sub> (Cu–Cu2) | 6                   | 3.59 ± 1.38  | 3.62               | 3.60             | 0.001               |

a less pronounced extend. However, the shoulder at the absorption edge is characteristic to pure Ni. The Cu XANES spectrum is nearly identical to the Cu film, confirming the presence of metallic Cu. XANES spectra of NiCu NPs with different sizes, shown in Figure S2d, Supporting Information, indicate an increase of Ni oxidation with decreasing size, while the Cu spectrum remains comparable to the Cu film. The magnitude of EXAFS oscillations for both Ni and Cu are shown in Figure 2c,d,

respectively. The EXAFS curve for Ni is combined with an fcc Ni and NiO fit (Figure 2c); the EXAFS curve for Cu with an fcc Cu fit (Figure 2d). The fit was performed for the first coordination shell, between 1.1 Å and 3.7 Å for Ni and in the first and second coordination sphere between 1.0 Å and 4.5 Å for Cu. The resulting coordination numbers and interatomic distances are given in Table 1. The Cu oscillation of the 16 nm NiCu NPs is in good agreement with the simulated structure of fcc Cu. The Ni oscillation can be fitted with the simulated structures of fcc Ni and NiO, while the coordination number is drastically lower than the ones for bulk Ni and NiO, indicating a low crystallinity in the Ni layer. These findings support the location of Cu in the center of the bimetallic NPs covered by metallic Ni and a protective passivation layer of NiO.

## 2.2. Influence of Reaction Parameters on NP Size

The preparation of well-defined nanostructures, including the size tuneability, is a critical factor achieved by a certain synthesis

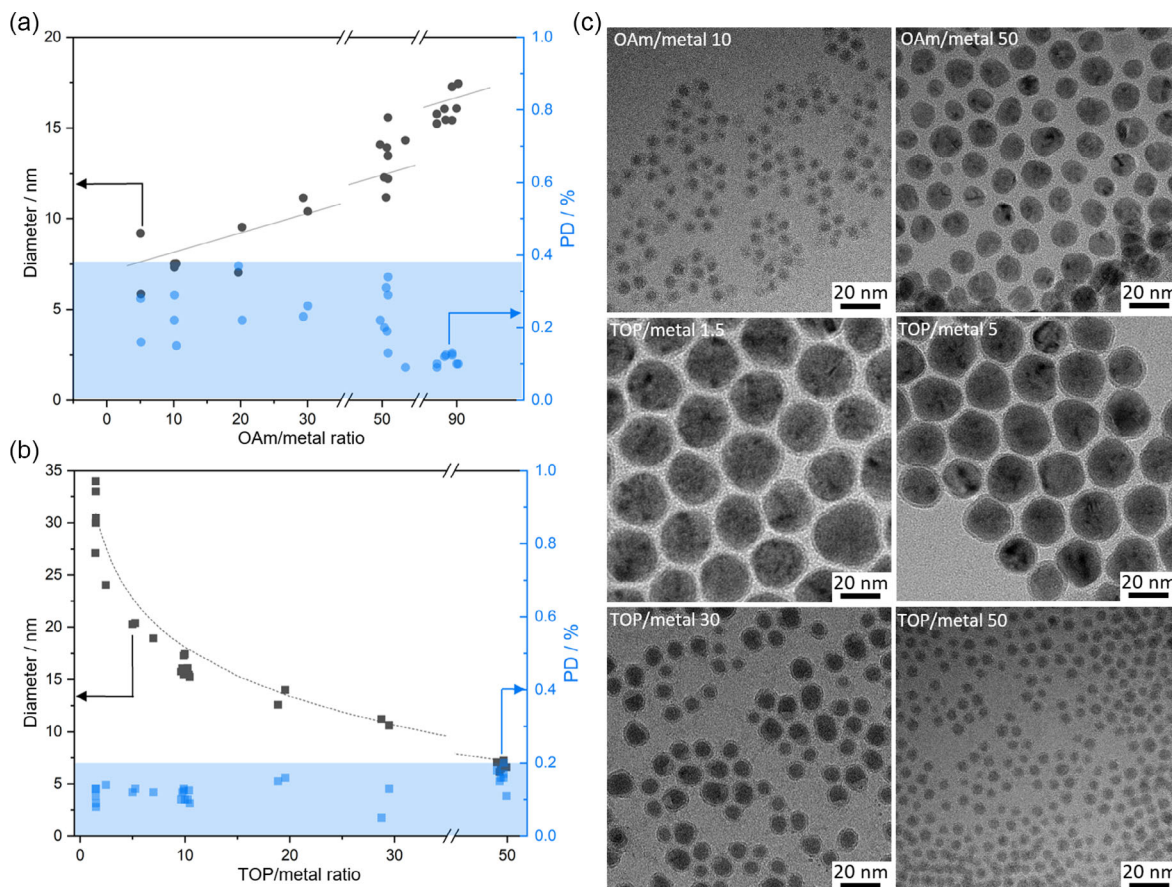


**Figure 3.** Impact of a) OAm and b) TOP amounts on the diameter of the NPs and c) exemplary TEM images of NPs synthesized with varying conditions. The TOP amount in the OAm study was kept at 10 eq, while DBE was added to keep the reaction volume at 5 mL. The OAm amount was adjusted according to the TOP amount in the TOP study without the addition of further solvent. Particle diameter and distribution were derived from SAXS and TEM studies.

method.<sup>[37]</sup> Therefore, we investigated the conditions of the synthesis method reported herein to optimize the tunability. Reaction conditions such as (1) the amount of reducing agent (OAm/metal ratios of 5–90) and (2) the amount of stabilizer (TOP/metal ratio within 1.5–50) were varied, while the metal salt concentration and the volume were kept stable. The corresponding synthesis conditions, particle diameters, and sample designations are summarized in Table S1, Supporting Information.

### 2.2.1. Amount of Reducing Agent (OAm/metal Ratio 5–90)

The studies concerning the impact of the OAm ratio to the metal salts on the particle diameter were conducted using additional cosolvent DBE to keep the reaction volume constant while adapting the amount of reducing agent, since it also acts as solvent. Dibenzyl ether (DBE) was considered as good cosolvent. It is available in high purity, not participating in the reaction, stable at high temperatures, and nontoxic. By increasing the amount of reducing agent from an OAm/metal ratio of 5–90 the NP diameter increases from 6 nm to 15 nm as shown in **Figure 3a**, based on SAXS data. The underlying SAXS data are shown in Figure S3, Supporting Information. 5 eq OAm lead to 6 nm particles (PD 16%), whereas 90 eq OAm lead to 16 nm particles (PD 11%) with comparable

polydispersity. During this increase, the polydispersity increases up to 40% in an OAm/metal ratio range of 20–50 while it is below 20% otherwise. The increase in polydispersity with increasing amount of reducing agent can be explained by the classical nucleation theory. Herein, the increase of reducing agent leads to a larger number of nucleation seeds, which offer the opportunity to grow with a larger distribution.

### 2.2.2. Amount of Stabilizer (TOP/metal Ratio 1.5–50)

By increasing the TOP/metal ratio from 1.5 to 50, the NP diameter decreases proportionally from 30 nm to 6 nm with a stable polydispersity lower than 20% as shown in **Figure 3b**, based on SAXS data. The underlying SAXS data are shown in Figure S4, Supporting Information. 1.5 eq lead to large particles with an average diameter of 30.9 nm and an average PD of 11% down to 6.8 nm particles (PD 16%) with 50 eq TOP. The NPs exhibit low dispersity and high sphericity in all cases as exemplarily depicted in the TEM images in **Figure 3c**. Due to the steric hindrance of TOP, we hypothesize that the particles are more effectively stabilized and thus protected against aggregation. All NPs produced are spherical and nearly monodisperse. Interestingly the herein observed size dependence is inverted compared to

the NiCu alloy nanospheres prepared by Liu et al., who found an increase of particle diameter from 7 nm to 27 nm by increasing the TOP/metal ratio from 0.6 eq to 3.4 eq, while keeping the OAm/metal ratio at 30 eq, and the Ni:Cu ratio at 1:1.<sup>[36]</sup>

The herein presented facile adapted synthesis method allows the tuning of the NiCu NPs diameter within 6 nm to 33 nm. Utilizing this method, a variety of NiCu NPs with varying diameters and Ni:Cu ratios were prepared and investigated concerning their catalytic activity for the RWGS reaction.

### 2.3. Nanostructure

ASAXS measurements were performed at eight X-ray photon energies between 7000 eV and 10 000 eV, mainly below the Ni- and Cu-K-edge X-ray energies. The effective electron density (EED) of the elements Ni, Cu, and NiO are calculated and shown in Figure 4a. The EEDs are showing strong variations near the two absorption edges caused by the anomalous corrections. The course and shape of the EEDs are indicating three outstanding energies: 8004 eV, 8330 eV, and 8973 eV. At 8004 eV, Cu and Ni show the same EED, while being much higher than NiO. At 8330 eV, the EED of Cu is significantly higher than Ni, which is still higher than NiO. The EED of Cu is not different to NiO at 8973 eV, but much lower than Ni. Moreover, the ratio between Ni and Cu inverts, comparing 8330 eV and 8973 eV. This knowledge will be used to identify from the relative effective electron density (REED) curves, in which structural parts the elements are enriched or diluted.<sup>[38]</sup>

Three scattering curves of about 17 nm NiCu NPs with an Ni:Cu ratio of 5:1, consequently labeled as 5NiCu-17, are shown in Figure 4b. These curves, measured just below the Ni-K edge, have very similar shapes, with a slight intensity shift. The resonant scattering curve calculated via the Stuhrmann method<sup>[39]</sup> (SI) is added.

The calculated Ni resonant curve (multiplied by a factor of 101 for better comparison) traces the shape and specifics of the scattering curves at the three energies up to  $q \approx 1.2 \text{ nm}^{-1}$ . Typically resonant curves are noisier due to the Stuhrmann data analysis method than its origin scattering curves of different photon energies.

However, the Ni resonant curve includes only the spatial distribution of Ni atoms. Therefore, this is a strong hint that the Ni atoms are distributed identically as in the scattering curves of each photon energy, resulting in an NiCu alloyed core with an Ni-enriched shell and an NiO outer shell.

As a cross-check and proof of principle to the proposed structure model, we have performed structure model fit approximations of a pure Cu core (Ni-free) with an Ni-enriched shell and an NiO outer shell on the obtained resonant Ni curve. This pure Cu core—Ni-enriched shell—NiO shell structure model shows significant differences to the resonant Ni curve and can therefore be excluded (see Figure S5, Supporting Information). Moreover, the NPs could not be modeled by a simple core and shell model, but an additional shell with a lower EED than the inner regions had to be added. Therefore, the scattering curves were approximated using a spherical core-shell-shell model. This model consists of a LogNorm distributed core and two shells without distribution surrounding the sphere, with shell 1 being the inner shell and shell 2 the outer shell. The total particle radius consists of the core radius and the thicknesses of the two shells. The REED, core radii, and shell thickness of seven samples are shown in Figure 5, and the underlying data are given in Table S6, Supporting Information, while the REED of the core is set to 1.

At 8004 eV, the REED of the core and inner shell is similar while the REED of the outer shell is lower, indicating the formation of an NiO shell, since the REED of NiO to Ni/Cu at 8004 eV is calculated as 0.77. At 8330 eV the inner shell's REED is lower than the core, indicating the occurrence of Ni atoms in the inner shell, since Cu has a higher REED than Ni at 8330 eV, while the REED of the outer shell is lower than both, core and inner shell. At 8973 eV, the REED of the inner shell is higher than the core, confirming the occurrence of Ni in the inner shell, due to the higher EED of Ni compared to Cu at 8973 eV given in Figure 4a.

The ratios of the REED of the inner and outer shell to the core are changing throughout the different NPs indicating a varying Cu content in the NP core, compared to an REED profile calculated for a theoretical NP with a 1:1 Ni:Cu core composition (see Figure S7, Supporting Information).

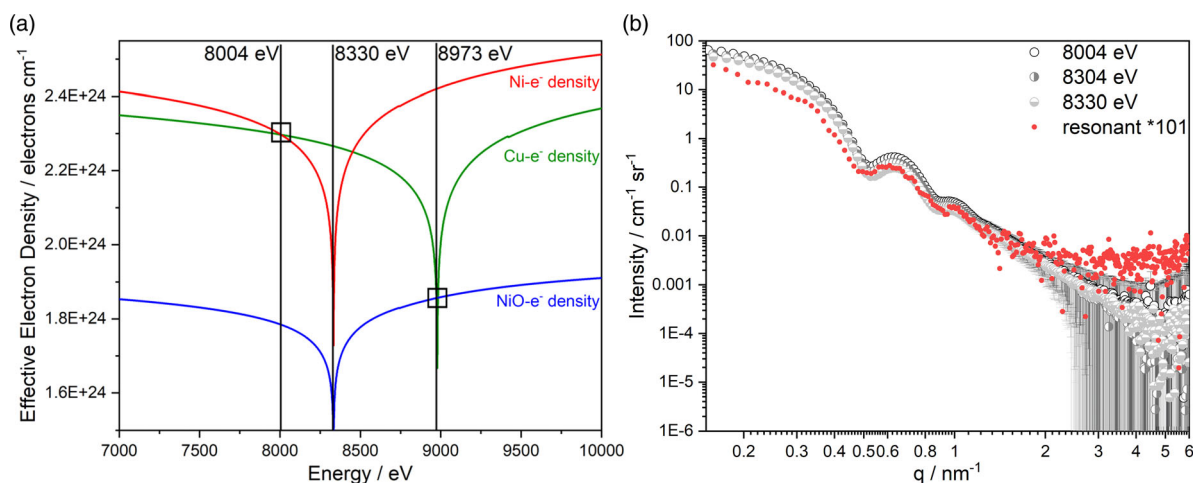


**Figure 4.** a) EEDs of Ni and Cu and NiO calculated around the X-ray K-absorption edges of Ni (8333 eV) and Cu (8979 eV), and b) scattering curves of 5NiCu-17 obtained at 8004 eV, 8304 eV, and 8330 eV compared with the resonant curve (red).

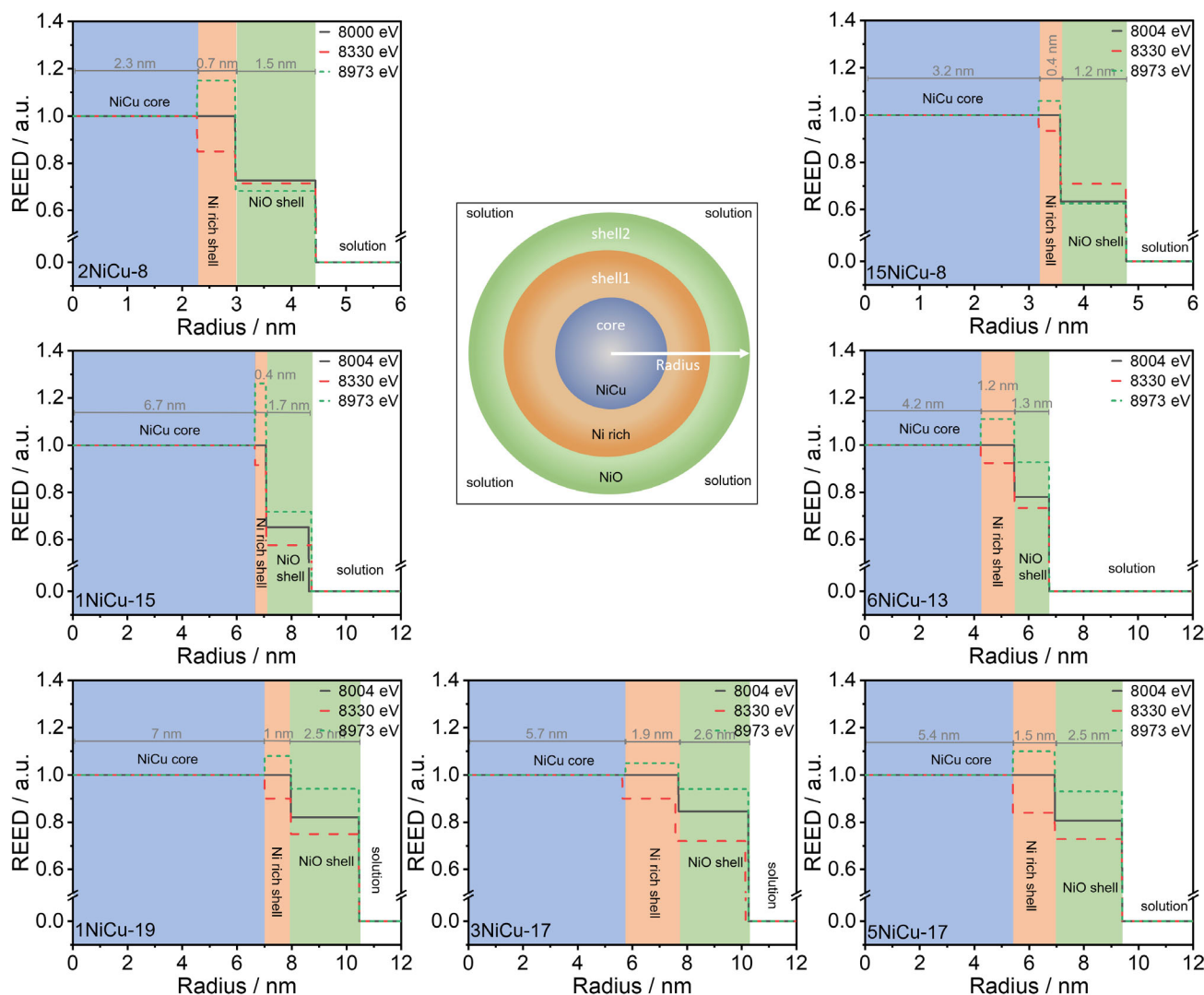


**Figure 5.** REED profiles of the NiCu NPs used for catalysis varying from 8 to 19 nm and from 15:1 to 1:1 Ni:Cu ratios. The REED profiles were achieved at 8000/8004 (black straight), 8330 (red straight), and 8973 eV (green dashed), and the areas of the NPs are indicated by blue for the CuNi core, orange for the inner shell 1, and green for the outer shell 2.

In the large 17 nm NPs, an increase of the core size with increasing Cu content is visible, while the NiO outer shell shows a thickness of 2.5 nm for all three samples.

In the 8 nm NPs, a lower Ni content in the core results (higher REED in the Ni-rich shell) in a thicker surrounding Ni shell (Ni-rich and NiO shell combined).

ASAXS analyses of the NPs, which were catalytically tested, resulted in a core-shell-shell structure. An NiCu alloy core is surrounded by an Ni enriched (or almost pure) layer, which is covered by an NiO-dominated outer and protecting shell.

XPS measurements of the NPs exemplary shown in **Figure 6a** for the Ni $2p_{3/2}$  region resulted in a mixture of Ni(II), Ni(0), and Cu(0) as given in **Table 2**. The fits of the Ni  $2p_{3/2}$  peaks were performed according to published parameters.<sup>[40]</sup> The same fit parameter was used for all high-resolution Ni  $2p$  spectra. As well, Cu  $2p$  spectra were fitted with well-established parameters.<sup>[41]</sup> The pronounced satellite structure of the Ni  $2p$  peaks shows

the dominant bivalent character of the Ni atoms, whereas such structure is missing for Cu  $2p$  (see **Figure S10**, Supporting Information). This agrees with metallic or monovalent Cu.

The XPS analyses of the 8 nm NiCu NPs result in a slightly lower but comparable Cu/Ni ratio as observed from ICP-MS bulk analysis, due to the information depth of XPS being half the size of the 8 nm NPs. With increasing Cu content the amount of Ni(0) increased, indicating a thinner NiO shell.

In the larger 15–19 nm NiCu NPs, significantly less Cu was detected compared with the bulk analysis, supporting the location of Cu in the NP core. The amount of detected Cu correlates with the amount of Cu determined by ICP-MS in the NiCu NPs. The Cu/Ni ratio expected according to the shell thicknesses given by ASAXS was calculated with SESA (input parameter given in **Table S9**, Supporting Information). Therefore, the size data obtained with ASAXS were used with a slightly simplified approach. For the core, the NiCu core and the enriched Ni shell

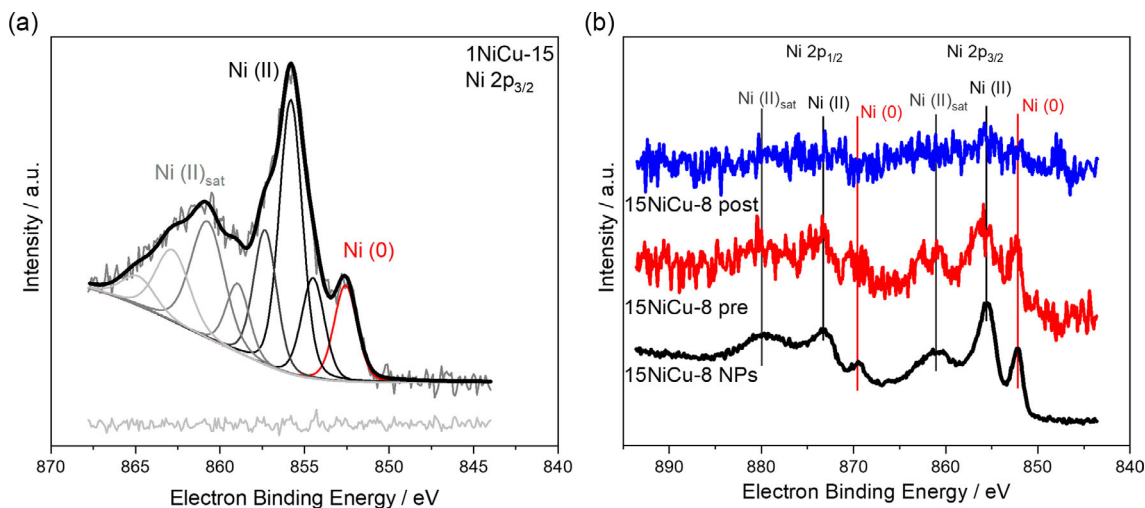


**Figure 6.** a) XPS spectrum of 15.0 nm NiCu NPs in the region of the Ni2p<sub>3/2</sub> states, b) XPS spectra of 8.0 nm NiCu NPs (black), supported on SiO<sub>2</sub> before catalysis (pre, red) and after catalysis (post, blue) in the region of the Ni2p states. The fitting parameters of the Ni 2p<sub>3/2</sub> peaks are provided in Table S8, Supporting Information.

**Table 2.** Cu/Ni ratios and the Ni(0)/Ni(II) ratios of NiCu NPs obtained with XPS and simulated in accordance with the ASAXS results. Uncertainties were calculated with a triangular distribution based on three different measurement points.

| sample   | Cu/Ni ratio <sup>a)</sup> | Cu/Ni ratio | Cu/Ni ratio simulated | Ni(0)/Ni(II) ratio | Ni(0)/Ni(II) ratio simulated |
|----------|---------------------------|-------------|-----------------------|--------------------|------------------------------|
| 5NiCu-17 | 0.18                      | 0.02 ± 0.01 | 0.02 ± 0.01           | 0.06 ± 0.01        | 0.11 ± 0.02                  |
| 3NiCu-17 | 0.28                      | 0.06 ± 0.05 | 0.03 ± 0.01           | 0.06 ± 0.02        | 0.11 ± 0.02                  |
| 1NiCu-19 | 0.70                      | 0.15 ± 0.03 | 0.05 ± 0.02           | 0.06 ± 0.02        | 0.08 ± 0.02                  |
| 1NiCu-15 | 0.78                      | 0.18 ± 0.02 | 0.09 ± 0.03           | 0.12 ± 0.02        | 0.17 ± 0.03                  |
| 6NiCu-13 | 0.16                      | 0.04 ± 0.01 | 0.06 ± 0.02           | 0.11 ± 0.02        | 0.39 ± 0.08                  |
| 15NiCu-8 | 0.07                      | 0.05 ± 0.01 | 0.03 ± 0.01           | 0.21 ± 0.02        | 0.40 ± 0.08                  |
| 2NiCu-8  | 0.47                      | 0.42 ± 0.12 | 0.07 ± 0.02           | 0.37 ± 0.04        | 0.17 ± 0.03                  |

<sup>a)</sup>ICP-MS data.

were combined. As composition the results obtained with ICP-MS were used. Furthermore, the NiO shell thickness was used as input parameter. Comparing these simulated and the experimentally determined ratios, similar or higher values were observed for the experimental results (Table 2). The simplification of the approach neglecting the Ni-rich shell would lead to a higher Ni amount in the simulation and could explain a lower Cu/Ni ratio in the experiments, but the opposite was observed. Recently, such differences between simulations and experiments were observed for core-shell NPs. It could be shown, that inhomogeneities in the shell led to these differences, for example, defects in the shell.<sup>[42]</sup> An outstanding high discrepancy between simulated and experimental results was observed for 2NiCu-8, which contradicts to a “simple” core-shell model. Intermixing or a defect-rich shell can be possible for the significant differences. For the Ni(0)/Ni(II) ratios lower values were observed in the experiment than expected from the ASAXS results. This difference hints to a more pronounced oxidation of the Ni shell for the

particles investigated with XPS than with ASAXS, which can be explained with a longer air contact of the particles before the XPS measurements compared with the ASAXS measurements, which were performed in suspension. Only for 2NiCu-8 a higher amount of metallic Ni was detected than expected, which confirms the assumption of a highly distorted core-shell structure for this kind of particles. The combination of a high Cu amount and a low amount of oxidized Ni in these 8 nm NPs suggests that Cu might prevent the oxidation of Ni. It must be noted that 6NiCu-13 shows a strikingly high amount of oxidized Ni, which hints that the Ni shell can be easily oxidized for these particles. For some samples, a higher degree of heterogeneity within the three measured positions was observed, possibly hinting that few pure NPs were formed. This analysis could not be conducted for the supported NPs due to the low concentration as shown in Figure 6b.

Ni atoms might be extracted from the core during that process and add to the NiO layer. For the simulation of the Cu/Ni ratio an uncertainty of 30% was assumed. The largest source of uncertainty is the EAL apart from the unclear composition of the NiCu core as discussed earlier and the theoretical atom cross sections (Scofield factors). The latter uncertainty source can be neglected for the determination of the Ni(0)/Ni(II) ratio. Thus, an uncertainty of 20% was assumed.

The XPS measurements confirm the location of Cu in the core of the NPs and the formation of an NiO shell on the surface of the NPs.

The XRD data suggested non-oxidized NiCu NPs, while additional investigation with XAS, ASAXS, and XPS revealed the formation of an NiO shell in addition to metallic Ni and Cu. Similar characteristics were found by An et al., who found no signs of oxidation in the XRD pattern, while the XPS measurements indicated the existence of Ni, Cu, O, and C.<sup>[34]</sup> The characterization of Ni and NiCu NPs with XRD to ensure the purity<sup>[36,43]</sup> seems therefore not to be overall sufficient, but it gains by the combination of different methods, which are not relying on the crystallinity.<sup>[34,44]</sup>



## 2.4. Catalytic Activity for the RWGS Reaction

As shown in the previous investigations, the core-shell particles consist of an NiCu core that is depleted of Cu on the outside, so that an NiO rich shell is formed. Ni as catalytic active element is well known for its ambivalent catalytic behavior with respect to the reductive conversion of CO<sub>2</sub> with hydrogen. On the one hand, CO via the RWGS reaction (Equation (1)) and, on the other hand, CH<sub>4</sub> via the Sabatier reaction (Equation (2)) can be formed. Two underlying reaction mechanisms are discussed in this respect: i) a redox mechanism which directly forms surface \*CO and ii) a hydrogen-assisted catalytic cycle via HCOO\* and \*COOH intermediates toward \*CO.<sup>[45]</sup> According to Chen et al.,<sup>[45]</sup> in turn, either the desorption of the formed CO (RWGS) or its hydrogenation to CH<sub>4</sub> (Sabatier reaction) takes place. The activation barriers for the \*CO desorption or its hydrogenation to CH<sub>4</sub> are directionally decisive. In the first case, CO is obtained, a crucial building block for the utilization of CO<sub>2</sub> as a raw material source. In the second case, the hydrogenated product CH<sub>4</sub> is obtained as a form of chemical hydrogen storage. The dependence of particle diameter of Ni catalysts was investigated in the hydrogen-assisted CO<sub>2</sub> reduction and as the particle diameter increases, the selectivity to methane increases and that to CO decreases.<sup>[14,32,33]</sup>

The reaction of CO<sub>2</sub> with H<sub>2</sub> is a popular field of research, especially nowadays. Interestingly, there are only few applications of core-shell catalysts for the Sabatier reaction

(Equation (2)) and almost no investigations regarding RWGS (Equation (1)), as was recognized in a recent review.<sup>[46,47]</sup> NiCu core-shell-shell NPs have never been studied for these two crucial reactions. To change that, the catalytic activity of bimetallic NiCu NPs for the conversion of CO<sub>2</sub> with hydrogen to CO (Equation (1)) was tested with a gas flow of 1:1 H<sub>2</sub>:CO<sub>2</sub> at ambient pressure of 1 bar. In addition, tests were carried out with a 4:1 mixture to exclude kinetic effects.

To test the intrinsic activity of the NiCu NPs, they were supported on porous SiO<sub>2</sub> by dry impregnation. They were evenly distributed on the surface of the porous SiO<sub>2</sub>, as shown in **Figure 7** for three representative catalysts. The structural properties of the supporting material and these catalysts are shown in **Table 3**. The porous SiO<sub>2</sub> supporting material exhibits a specific

**Table 3.** Structural properties of NiCu-SiO<sub>2</sub> catalysts.

|                  | NP diameter [nm] | Loading <sup>a)</sup> [wt%] | S <sub>BET</sub> <sup>b)</sup> [m <sup>2</sup> g <sup>-1</sup> ] | Pore size <sup>c)</sup> [nm] | Specific pore volume <sup>c)</sup> [mL g <sup>-1</sup> ] |
|------------------|------------------|-----------------------------|--|------------------------------|--|
| SiO <sub>2</sub> | –                | –                           | 23.6   | 157.1                        | 1.06   |
| 15NiCu-8         | 8.0              | 1.21                        | 22.5   | 154.8                        | 1.02   |
| 6NiCu-13         | 12.7             | 0.91                        | 23.1   | 155.2                        | 1.03   |
| 5NiCu-31         | 31.0             | 0.98                        | 22.7   | 156.7                        | 1.02   |

<sup>a)</sup>determined by ICP-MS; <sup>b)</sup>determined via N<sub>2</sub> sorption; <sup>c)</sup>determined via MIP.

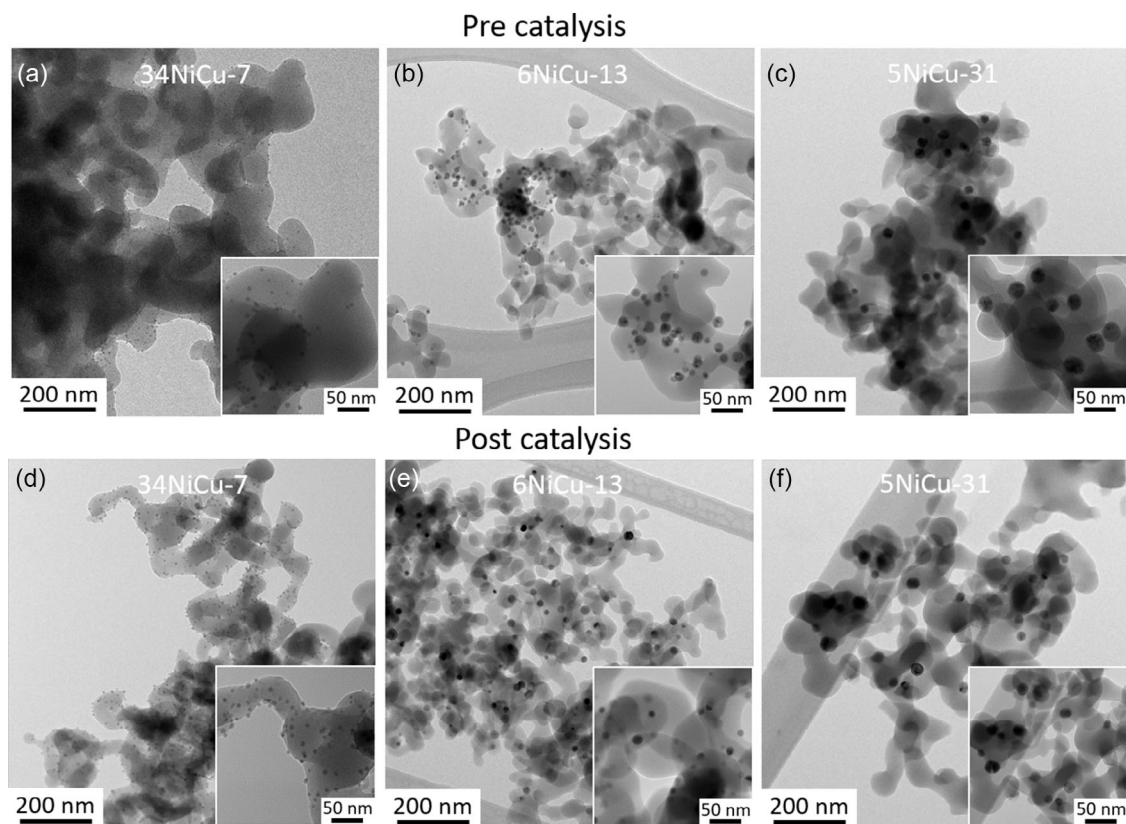


**Figure 7.** TEM images of NiCu NPs on SiO<sub>2</sub> catalysts a–c) pre-catalysis and d–f) post-catalysis of 7 nm NiCu NPs with an Ni:Cu ratio of 34 (left), 12.7 nm NPs with an Ni:Cu ratio of 6.2 (middle), and 31 nm NPs with an Ni:Cu ratio of 4.9.

surface area determined by BET of  $23.6 \text{ m}^2 \text{ g}^{-1}$ , a pore size of 157 nm and a specific pore volume of  $1.1 \text{ mL g}^{-1}$ . The specific surface did not change upon supporting with NPs and the mean pore size was comparable. The specific pore volume decreased slightly upon supporting with NPs, since the NPs locate on the inner pore surface of the porous  $\text{SiO}_2$  as the pore size distribution in Figure S11, Supporting Information, supports.

The  $\text{CO}_2$  conversion at  $500^\circ\text{C}$  of all prepared catalysts in dependence of their diameter are shown in Figure S12, Supporting Information. One can see a slight dependence of the  $\text{CO}_2$  conversion rate on the particle diameter. Particles of a diameter of approximately 8 nm convert  $21\text{--}46 \text{ mmol}_{\text{CO}_2} \text{ min}^{-1} \text{ g}_{\text{NP}}^{-1}$ , while the conversion rate for particles in the diameter range from 13 nm to 31 nm convert  $\text{CO}_2$  between 60 and  $77 \text{ mmol}_{\text{CO}_2} \text{ min}^{-1} \text{ g}_{\text{NP}}^{-1}$ .

Importantly, the CO selectivity lies between 99% and 100% compared to  $\text{CH}_4$ , as shown in Figure S12, Supporting Information, for all catalysts. This result could also be confirmed with an  $\text{H}_2:\text{CO}_2 = 4:1$  mixture (Figure 8). From previous studies it is known, that the selectivity to methane reaches higher values at lower temperatures and decreases with increasing reaction temperature.<sup>[8,15]</sup> Wu et al. have correlated the relationship between particle diameter and selectivity.<sup>[14]</sup> During hydrogenation experiments at 623 K sub-nm particles showed increased selectivity to CO. Particles of 9 nm, however, formed approximately 90% methane. Liu et al. and Chen et al. investigated the relationship between diameter and selectivity at 723 K and 773 K and found the same dependencies.<sup>[32,33]</sup> Figure 8 shows these literature data and compares the unusual selectivities we observed. Contrary to previous observations, we see nearly 100% selectivity for CO for all particle diameters.

Currently, we see the reason for the independence of the selectivity from the particle size in the surface structure of the core-shell particles. The detailed characterization has shown that the particles mainly consist of NiO on the surface. Some catalysts

have an increased Cu content (1NiCu-19, 1NiCu-15, and 2NiCu-8), but this correlates with increased activity, if at all, only in the smallest particles studied. The selectivity is not affected by different Cu contents. Thus, the disturbance of the surface structure by Cu is not likely to be the main cause of our observation. Rather, we see the origin of the nearly perfect selectivity for CO in the primary particle size, as shown in Figure S2b. The crystallite surfaces presented to the outside are very small single crystals. A generally strong disturbance of the surface structure can also be assumed, which separates these single crystals from each other. In the catalytic reaction of  $\text{CO}_2$  with  $\text{H}_2$ , this surface structure is likely the cause of pure selectivity to CO.

### 3. Conclusion

A facile and easy, adapted synthesis route for the preparation of nearly monodisperse bimetallic NiCu NPs is presented. The NP size could be changed by adjusting the amount of reducing and stabilizing agent and the Ni:Cu ratio by adapting the metal precursor ratio. The NPs were thoroughly investigated with various methods, revealing a core-shell-shell structure with a Cu-Ni alloy in the core, an Ni-rich inner shell, and an outer shell of NiO. XANES measurements and the XPS surface analysis supported the ASAXS results, revealing the power of combining analytical methods for an in-detail characterization of nanomaterials. The bimetallic NiCu NPs show a very good catalytic activity for the RWGS reaction converting  $\text{CO}_2$  into CO. The herein tested NiCu NPs showed a size and Cu content independent nearly 100% selectivity to CO, thus being promising materials for the incorporation into the Power-to-Syngas cycle. XPS, ASAXS, and TEM measurements indicated a disturbed NiO surface of the NPs, which most likely causes the high selectivity to CO.

The knowledge of the nanomaterials structure and composition is key for scientific progress in the field of catalysis, which is only achievable with the combination of various analytical methods.

### 4. Experimental Section

**Synthesis of Nickel-Copper NPs:** Oleylamine (OAm, Acros, C18-content 80%–90%), trioctylphosphine (TOP, abcr, 97%; Sigma Aldrich, 90%), nickel(II) acetylacetonate ( $\text{Ni}(\text{acac})_2$ , Acros, 96%), copper(II) acetylacetonate ( $\text{Cu}(\text{acac})_2$ , Acros, 96%), dibenzyl ether (DBE, Acros, 99%), ethanol (Chemsolute, 99.9%), and n-hexane (Chemsolute, 99%) were used as received.

All reactions were carried out in 20 mL glass vials sealed by a screw cap with a butyl/PTFE septum under a nitrogen atmosphere. These vials were heated using a dry block heater (IKA, Staufen, Germany, DB 5.6) on a heating plate (IKA) for 10 min at  $100^\circ\text{C}$  and 2 h at  $220^\circ\text{C}$ . All syntheses were carried out with 5 mL total volume to prevent the interference of any concentration or volume effects on the heating rate. The typical synthesis procedure was described in the study by Heilmann et al.<sup>[25]</sup> This procedure was adapted by adding  $\text{Cu}(\text{acac})_2$  to  $\text{Ni}(\text{acac})_2$  in OAm at room temperature. The amount of OAm was varied within 5–90 equivalents (eq) and TOP within 1.5–50 eq to the total amount of metal salt. A detailed overview of the used reaction parameters is given in Table S1, Supporting Information.

**Catalyst Preparation:** In several steps (detailed in the following section), the NP dispersions were dry impregnated on porous  $\text{SiO}_2$  (Grace GmbH, Worms, Germany) until an approximate loading of 1 wt% NPs was reached. This process includes the addition of a small amount of NP

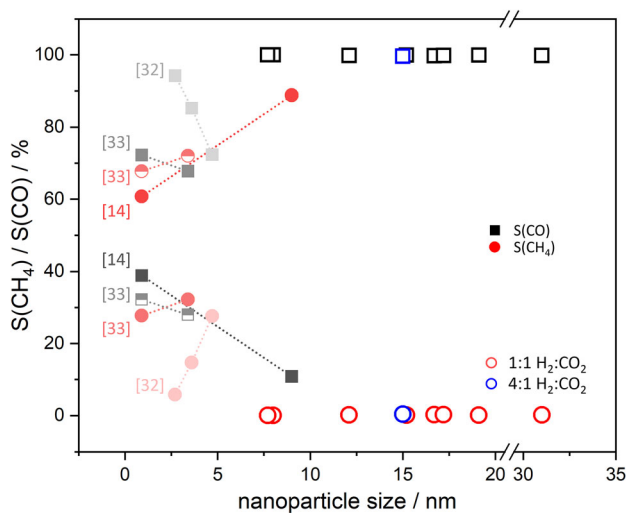


**Figure 8.** Catalytic reaction of  $\text{CO}_2$  with  $\text{H}_2$  over Ni particles on  $\text{SiO}_2$ : NP diameter dependent selectivity for CO (squares) and  $\text{CH}_4$  (circles) with  $\text{H}_2:\text{CO}_2$  ratios of 1:1 (red/black) and 4:1 (blue). Reference selectivities are taken from Wu et al. (623 K)<sup>[14]</sup>, Chen et al. (773 K)<sup>[32]</sup>, and Liu et al. (573 K open circle, 725 K full circle)<sup>[33]</sup>.

dispersion ( $\approx 2$  mL per 5 g SiO<sub>2</sub>) which diffuses into the pores and leaves the material still dry. The solvent was evaporated at 70 °C in an oven for 1 h, after which the process was repeated. After drying, the supported NPs were washed several times with ethanol and dried. Small portions of the catalysts (5–10 mg) were dissolved in 2 mL chloric acid (sub-boiling distilled), centrifuged, and decanted. The metal loading and the molar ratio of Ni and Cu were determined with inductively coupled plasma mass spectrometry (ICP-MS).

**SAXS Measurements:** Small-angle X-ray scattering (SAXS) curves of the NiCu NPs were collected on a Kratky-type SAXS instrument (SAXSess, Anton Paar, Graz, Austria), equipped with a sealed X-ray tube ( $\lambda_{\text{CuK}\alpha} = 0.1542$  nm) and a microstrip X-ray detector (Mythen2 R detector system, Dectris, Baden-Daettwil, Switzerland). Samples were filled in a vacuum-tight glass capillary (diameter: 1 mm) and measured with an acquisition time of 10 min. The measured intensity was corrected for background contributions and slit smearing effect using the software package SAXSquant4.2 (Anton Paar). The magnitude of the scattering vector  $q$  was defined in terms of the scattering angle  $2\theta$  and the wavelength  $\lambda$  of the incoming beam; thus,  $q = 4\pi/\lambda \cdot \sin \theta$ . SAXS data analysis was performed with the SASfit program package 0.94.11.<sup>[35]</sup>

**ASAXS Measurements:** ASAXS measurements were performed at the four-crystal monochromator (FCM) beamline of the Physikalisch-Technische Bundesanstalt (PTB), the German National Metrology Institute,<sup>[48]</sup> at the BESSY II synchrotron (Helmholtz-Zentrum Berlin für Materialien und Energie [HZB], Berlin, Germany). The beamline was combined with the HZB ASAXS instrument.<sup>[49]</sup> The incoming photon flux was monitored with an 8  $\mu\text{m}$  semitransparent photodiode operating in transmission mode. The beam transmitted through the sample was measured with a photodiode inside the beamstop in front of the scattering detector. The SAXS patterns were recorded with a 2D X-ray hybrid pixel detector (Pilatus 1M, Dectris Ltd., Switzerland)<sup>[50]</sup> at two different distances ( $\approx 0.8$  m and  $\approx 3.8$  m) at eight photon energies between 7000 eV and 10 000 eV. The fundamental theoretical aspects of ASAXS and the choice of X-ray energies are given in the Supporting Information.

The samples were measured in sealed borosilicate glass capillaries of 1 mm diameter with an acquisition time of 600 s each. The magnitude of the scattering vector was calibrated using the known  $d$ -spacing of measured silver behenate. To convert all measured curves to absolute differential scattering cross sections, glassy carbon was used as calibrant and additionally measured. The collected 2D raw scattering data patterns were corrected for possible variations in the incoming photon flux, sample transmission, scattering background, and geometrical effects by spherical projection. The scattering background arising from beamline components was measured within each sample sequence using an empty capillary. The scattering images were azimuthally averaged to scattering curves around the beam center.

**XPS Measurements:** The samples were prepared by dropping the NP suspension on a clean Si wafer, previously treated with several solvents and a UV Ozon Cleaner as described in the study by Bennet et al.,<sup>[51]</sup> and dried in air. The XPS measurements were conducted with an AXIS Ultra DLD photoelectron spectrometer (Kratos Analytical, Manchester, UK) with monochromatic Al K $\alpha$  radiation ( $h\nu = 1486.6$  eV) at a pressure of approximately  $5 \times 10^{-9}$  mbar. The electron emission angle was 0° and the source-to-analyzer angle was 60°. The binding energy scale of the instrument was calibrated following a Kratos Analytical procedure which uses ISO 15 472 binding energy data.<sup>[52]</sup> The XPS spectra were recorded in the fixed analyzer transmission mode, in the hybrid lens mode and the slot mode providing approximately a  $300 \times 700 \mu\text{m}^2$  analysis area, using a charge neutralizer. Survey spectra were measured with a pass energy of 80 eV; high-resolution spectra were recorded with a pass energy of 20 eV. The survey spectra were used for the quantification. Therefore, the areas of the main peak of each component were normalized with the element-specific Scofield factors as atomic cross sections, the inelastic mean free pathway of the photoelectrons, and the spectrometer-specific transmission function. For the background of the peaks, a modified Tougaard background was used. For the determination of the valence states, the high-resolution spectra were fitted with the sum of a Gaussian–Lorentzian curve. The uncertainty of the electron binding energy is estimated within  $\pm 0.2$  eV.

The intensities of the XPS spectra were simulated with SESSA v.2.0.<sup>[53]</sup> SESSA is a standard database distributed by the National Institute of Standards and Technologies (NIST) which calculates intensities from a statistically relevant large number of photoelectron trajectories. Thereby, the geometry of the sample was considered. The simulations were performed iteratively. The key parameter for the accuracy of the simulations was the effective attenuation length (EAL) determined with SESSA. The EAL corresponds to the inelastic mean free path, versus the average distance of an electron between successive inelastic collisions, corrected for the contribution of elastic scattering effects.<sup>[54]</sup> Inelastic mean free paths were obtained with the predictive TPP-2M formula,<sup>[55]</sup> and elastic scattering cross sections were obtained from NIST database.<sup>[56]</sup> Depending on the physical model used for the calculations differences up to 10% were observed.<sup>[57,58]</sup>

**TEM and STEM-EDS Measurements:** Samples for TEM and scanning transmission electron microscopy-X-ray spectroscopy (STEM-EDS) analyses were prepared by dropping the NiCu NP solution on a lacey carbon-coated Cu grid and allowing the solvent to evaporate. Catalyst dispersions in ethanol were sprayed in TEM grids for TEM measurements using pressurized argon. TEM and STEM-EDS analyses were performed on a Talos F200S microscope (Thermo Scientific, 200 kV).

**XRD Measurements:** Routine X-ray diffraction (XRD) measurements were performed on a laboratory diffractometer (D8 Discover, Bruker AXS) in transmission geometry (Cu K $\alpha$  ( $\lambda = 1.54056$  Å)). The XRD measurements of colloidal NiCu NP dispersions were performed at the  $\mu\text{Spot}$  beamline<sup>[59]</sup> at the BESSY II synchrotron (HZB, Berlin, Germany) utilizing an acoustic levitator as sample holder, as described in previous studies for example by Wolf et al.<sup>[60]</sup> A monochromatized (Si 111) X-ray beam with a wavelength of 0.712 Å and a beam size of 100  $\mu\text{m}$  was used. The X-ray radiation was detected at a working distance of 200 mm with a 2D X-ray detector (EIGER 9M, 3110  $\times$  3269 pixels). The diffraction images obtained were processed and converted into diagrams of scattered intensities versus the scattering vector  $q$  using DPDAK.<sup>[61]</sup>

**XANES and EXAFS Measurements:** X-ray near edge absorption spectroscopy (XANES) and extended X-ray absorption fine structure (EXAFS) investigations were performed at the BAMline at BESSY II. The samples were prepared by applying a colloidal NiCu NP dispersion to boron nitride (BN), evaporating the solvent, reducing the size of the resulting solid specimen with a mortar and pestle, and pressing to a defined layer thickness of 1 mm. The catalyst material was without addition of BN pressed to a layer thickness of 1 mm. The XAS measurements were conducted at the Ni K-edge between 8183 eV and 8850 eV and at the Cu K-edge between 8824 eV and 9948 eV. The determination of the absorption edge, the pre- and post-edge normalization of the absorption, the transformation of the experimental EXAFS data into  $k$ -space (wavenumber of the photoelectron), and the determination of the EXAFS oscillations  $\chi(k)$  were performed with the program Athena. The evaluation of the  $\chi(k)$  function and the simulation of the scattering paths of the photoelectron based on model Ni fcc (ICSD 64 989), NiO (ICSD 184 918), and Cu fcc (ICSD 627 113) were performed with the program Artemis. Both of which belong to the Software package IFEFFIT (Demeter).<sup>[62]</sup>

**Pore Structure Analysis:** Gas sorption with nitrogen at 77 K with an ASAP 2020 (Micromeritics) was used to determine the specific surface area from a multipoint adsorption isotherm branch with the BET (Brunauer–Emmitt–Teller) calculation model (relative pressure range of  $0.05 < p/p_0 < 0.2$ ) according to DIN ISO 9277:2014.<sup>[63]</sup> Mercury intrusion porosimetry (MIP) was used for further characterization of the pore size distribution (most frequent), the specific pore volume and the porosity with an Autopore V (Micromeritics) according to ISO 15 901-1:2016-04.<sup>[64]</sup>

**Mass Spectrometry Measurements:** ICP-MS measurements were performed with an iCAP Qc ICP-MS (Thermo Scientific GmbH), equipped with a Teflon nebulizer, a quartz torch, and a spray chamber. Sample preparation was conducted by dissolving 5 mg catalyst in 2 mL chloric acid, separating the supporting material by centrifugation, after which 1:10 and 1:100 dilutions were measured.

**Catalytic Testing:** The catalytic activity for the RWGS reaction was tested in a horizontal fixed bed plug flow reactor at atmospheric pressure and at 500 °C. Typically, 100 mg of catalyst was placed in a quartz tube with an

inner diameter of 8 mm and fixed with quartz wool. Behind the catalyst bed, the inner diameter of the reactor decreases to 4 mm. The temperature was controlled by a thermocouple in the middle of the catalyst bed and measurements were performed after reaching steady state. The reactant gas mixture consisted of 1:1 CO<sub>2</sub>:H<sub>2</sub> (1:4 CO<sub>2</sub>:H<sub>2</sub>), and the gas flow passing the reactor was adjusted using mass flow controllers (MKS-Instruments, Andover, MA, USA) and set to a total flow rate of 25 mL min<sup>-1</sup>. The online gas analysis was carried out with an FT-IR spectrometer (CX1000, Ansyco, Karlsruhe, Germany) and the CALCMET software, which uses reference spectra of the single compounds at different concentrations. Spectra were averaged over the period of 1 min prior to analysis. The conversion of CO<sub>2</sub> (X<sub>CO2</sub>) and the yield of CO (Y<sub>CO</sub>), as well as the selectivity (S<sub>CO</sub> and SCH4), were then calculated by the following equations

$$X_{\text{CO}_2}(\%) = \frac{[\text{CO}_2]_{\text{in}} - [\text{CO}_2]_{\text{out}}}{[\text{CO}_2]_{\text{in}}} \cdot 100\% \quad (3)$$

$$Y_{\text{CO}}(\%) = \frac{[\text{CO}]_{\text{out}} - [\text{CO}]_{\text{in}}}{[\text{CO}_2]_{\text{in}}} \cdot 100\% \quad (4)$$

$$S_{\text{CO}}(\%) = \frac{Y_{\text{CO}}}{X_{\text{CO}_2}} \cdot 100\% \quad (5)$$

## Supporting Information

Supporting Information is available from the Wiley Online Library or from the author.

## Acknowledgements

The authors gratefully acknowledge the support of the PTB FCM-beamline staffs, Christian Gollwitzer and Dieter Skroblin. The authors also thank Antje Cossmer for the conduction of the ICP-MS measurements, Jörg Stockmann for the XPS measurements, and Annett Zimathies for the MIP and gas-sorption measurements.

Open access funding enabled and organized by Projekt DEAL.

## Conflict of Interest

The authors declare no conflict of interest.

## Data Availability Statement

The data that support the findings of this study are available from the corresponding author upon reasonable request.

## Keywords

ASAXS, catalysis, core-shell, nanoparticles, reverse water-gas shift reaction, TEM, XAFS

Received: September 26, 2021

Revised: December 20, 2021

Published online:

- [1] N. L. Rosi, C. A. Mirkin, *Chem. Rev.* **2005**, *105*, 1547.  
 [2] T. S. Bedwell, M. J. Whitcombe, *Anal. Bioanal. Chem.* **2016**, *408*, 1735.  
 [3] E. K. Athanassiou, R. N. Grass, W. J. Stark, *Nanotechnology* **2006**, *17*, 1668.

- [4] M. Mabrouk, R. M. Abd El-Wahab, H. H. Beherei, M. M. Selim, D. B. Das, *Int. J. Pharm.* **2020**, *587*, 119658.  
 [5] M. Pan, J. Yang, K. Liu, Z. Yin, T. Ma, S. Liu, L. Xu, S. Wang, *Nanomaterials* **2020**, *10* 209.  
 [6] S. Y. Bae, J. Mahmood, I. Y. Jeon, J. B. Baek, *Nanoscale Horiz.* **2020**, *5*, 43.  
 [7] H. Y. Guo, Z. W. Fang, H. Li, D. Fernandez, G. Henkelman, S. M. Humphrey, G. H. Yu, *ACS Nano* **2019**, *13*, 13225.  
 [8] A. Ranjbar, A. Irankhah, S. F. Aghamiri, *J. Environ. Chem. Eng.* **2018**, *6*, 4945.  
 [9] M. Gong, D.-Y. Wang, C.-C. Chen, B.-J. Hwang, H. Dai, *Nano Res.* **2016**, *9*, 28.  
 [10] A. Menazea, M. Ahmed, *J. Mol. Struct.* **2020**, *1218*, 128536.  
 [11] C. Du, X. Gao, W. Chen, *Chin. J. Catal.* **2016**, *37*, 1049.  
 [12] P. Frontera, A. Macario, M. Ferraro, P. Antonucci, *Catalysts* **2017**, *7*, 28.  
 [13] Y. A. Daza, J. N. Kuhn, *RSC Adv.* **2016**, *6*, 49675.  
 [14] H. C. Wu, Y. C. Chang, J. H. Wu, J. H. Lin, I. K. Lin, C. S. Chen, *Catal. Sci. Technol.* **2015**, *5* 4154-.  
 [15] L. Wang, H. Liu, Y. Liu, Y. Chen, S. Yang, *J. Rare Earths* **2013**, *31*, 559.  
 [16] B. Lu, Z. Zhang, X. Li, C. Luo, Y. Xu, L. Zhang, *Fuel* **2020**, 276.  
 [17] K. Ding, L. Liu, Y. Cao, X. Yan, H. Wei, Z. Guo, *Int. J. Hydrogen Energy* **2014**, *39*, 7326.  
 [18] N. Lasemi, G. Rupprechter, *Catalysts* **2020**, *10*, 1453.  
 [19] R. K. Ramachandran, J. Dendooven, M. Filez, V. V. Galvita, H. Poelman, E. Solano, M. M. Minjauw, K. Devloo-Casier, E. Fonda, D. Hermida-Merino, W. Bras, G. B. Marin, C. Detavernier, *ACS Nano* **2016**, *10*, 8770.  
 [20] T. Som, R. Wendt, S. Raoux, J. L. Jordan-Sweet, M. Wollgarten, K. Rademann, *MRS Online Proc. Lib.* **2015**, *1802*, 13.  
 [21] A. Gołębiewska, W. Lisowski, M. Jarek, G. Nowaczyk, M. Michalska, S. Jurga, A. Zaleska-Medynska, *Mol. Catal.* **2017**, *442*, 154.  
 [22] R. Ghosh Chaudhuri, S. Paria, *Chem. Rev.* **2012**, *112*, 2373.  
 [23] N.-D. Jaji, H. L. Lee, M. H. Hussin, H. M. Akil, M. R. Zakaria, M. B. H. Othman, *Nanotechnol. Rev.* **2020**, *9*, 1456.  
 [24] A. P. LaGrow, B. Ingham, M. F. Toney, R. D. Tilley, *J. Phys. Chem. C* **2013**, *117*, 16709.  
 [25] M. Heilmann, H. Kulla, C. Prinz, R. Bienert, U. Reinholz, A. Guilherme Buzanich, F. Emmerling, *Nanomaterials* **2020**, *10*, 713.  
 [26] S. Carencu, C. D. Boissière, L. Nicole, C. M. Sanchez, P. Le Floch, N. Mézailles, *Chem. Mater.* **2010**, *22*, 1340.  
 [27] Z. C. Wang, Y. Z. Chen, D. Q. Zeng, Q. F. Zhang, D. L. Peng, *Crystengcomm* **2016**, *18*, 1295.  
 [28] S. Carencu, *Chem. Rec.* **2018**, *18*, 1114.  
 [29] K. Guo, Y. Ding, J. Luo, M. Gu, Z. Yu, *ACS Appl. Energy Mater.* **2019**, *2*, 5851.  
 [30] A. L. Lapidus, N. A. Gaidai, N. V. Nekrasov, L. A. Tishkova, Y. A. Agafonov, T. N. Myshenkova, *Pet. Chem.* **2007**, *47*, 75.  
 [31] G. Centi, S. Perathoner, *Greenhouse Gases Sci. Technol.* **2011**, *1*, 21.  
 [32] C.-S. Chen, C. S. Budi, H.-C. Wu, D. Saikia, H.-M. Kao, *ACS Catal.* **2017**, *7*, 8367.  
 [33] M.-H. Liu, H.-A. Chen, C.-S. Chen, J.-H. Wu, H.-C. Wu, C.-M. Yang, *Nanoscale* **2019**, *11*, 20741.  
 [34] Y. An, H. Ijaz, M. Huang, J. Qu, S. Hu, *Dalton Trans.* **2020**, *49*, 1646.  
 [35] I. Breßler, J. Kohlbrecher, A. F. Thünemann, *J. Appl. Crystallogr.* **2015**, *48*, 1587.  
 [36] J. Liu, Y. Zheng, S. Hou, *RSC Advances* **2017**, *7*, 37823.  
 [37] A. Vivien, M. Guillaumont, L. Meziane, C. Salzemann, C. Aubert, S. Halbert, H. Gérard, M. Petit, C. Petit, *Chem. Mater.* **2019**, *31*, 960.  
 [38] A. Hoell, Z. Varga, V. S. Raghuwanshi, M. Krumrey, C. Bocker, C. Rüssel, *J. Appl. Crystall.* **2014**, *47*, 60.

- [39] H. Stuhmann, *Characterization of Polymers in the Solid State II: Synchrotron Radiation, X-Ray Scattering and Electron Microscopy*, Springer, Berlin **1985**, pp. 123–163.
- [40] M. C. Biesinger, B. P. Payne, A. P. Groszover, L. W. M. Lau, A. R. Gerson, R. S. C. Smart, *Appl. Surf. Sci.* **2011**, 257, 2717.
- [41] M. C. Biesinger, L. W. M. Lau, A. R. Gerson, R. S. C. Smart, *Appl. Surf. Sci.* **2010**, 257, 887.
- [42] A. Müller, T. Heinrich, S. Tougaard, W. S. Werner, M. Hronek, V. Kunz, J. R. Radnik, J. R. M. Stockmann, V.-D. Hodoroba, S. Benemann, *J. Phys. Chem. C* **2019**, 123, 29765.
- [43] Y. Shen, Y. Zhou, D. Wang, X. Wu, J. Li, J. Xi, *Adv. Energy Mater.* **2018**, 8, 1701759.
- [44] H. Winnischofer, T. C. Rocha, W. C. Nunes, L. M. Socolovsky, M. Knobel, D. Zanchet, *ACS Nano* **2008**, 2, 1313.
- [45] X. Chen, X. Su, H.-Y. Su, X. Liu, S. Miao, Y. Zhao, K. Sun, Y. Huang, T. Zhang, *ACS Catal.* **2017**, 7, 4613.
- [46] S. Das, J. Perez-Ramirez, J. Gong, N. Dewangan, K. Hidajat, B. C. Gates, S. Kawi, *Chem. Soc. Rev.* **2020**, 49, 2937.
- [47] D. T. Cromer, D. Liberman, *J. Chem. Phys.* **1970**, 53, 1891.
- [48] M. Krumrey, G. Ulm, *Nucl. Instrum. Methods Phys. Res. Sect. A* **2001**, 467, 1175.
- [49] A. Hoell, I. Zizak, H. Bieder, L. Mokrani, DE102006029449 **2007**.
- [50] J. Wernecke, C. Gollwitzer, P. Müller, M. Krumrey, *J. Synchrotron Radiat.* **2014**, 21, 529.
- [51] F. Bennet, A. Müller, J. Radnik, Y. Hachenberger, H. Jungnickel, P. Laue, A. Luch, J. Tentschert, *JOVE-J. Visualized Exp.* **2020**, 163, 61758.
- [52] ISO 15472:2010, International Organisation for Standardization, Geneva, **2010**.
- [53] W. Smekal, W. S. Werner, C. J. Powell, *Surf. Interface Anal.* **2005**, 37, 1059.
- [54] C. J. Powell, A. Jablonski, *Surf. Interface Anal.* **2002**, 33, 211.
- [55] S. Tanuma, C. Powell, D. Penn, *Surf. Interface Anal.* **2011**, 43, 689.
- [56] A. Jablonski, F. Salvat, C. Powell, *NIST Stand. Ref. Database* **2010**, 64.
- [57] C. Powell, A. Jablonski, *Nucl. Instrum. Methods Phys. Res. Sect. A* **2009**, 601, 54.
- [58] C. J. Powell, A. Jablonski, W. S. Werner, W. Smekal, *Appl. Surf. Sci.* **2005**, 239, 470.
- [59] O. Paris, C. Li, S. Siegel, G. Weseloh, F. Emmerling, H. Riesemeier, A. Erko, P. Fratzl, *J. Appl. Crystall.* **2007**, 40, 466.
- [60] S. E. Wolf, J. Leiterer, M. Kappl, F. Emmerling, W. Tremel, *J. Am. Chem. Soc.* **2008**, 130, 12342.
- [61] G. Benecke, W. Wagermaier, C. Li, M. Schwartzkopf, G. Flucke, R. Hoerth, I. Zizak, M. Burghammer, E. Metwalli, P. Muller-Buschbaum, M. Trebbin, S. Forster, O. Paris, S. V. Roth, P. Fratzl, *J. Appl. Crystall.* **2014**, 47, 1797.
- [62] B. Ravel, M. Newville, *J. Synchrotron Rad.* **2005**, 12, 537.
- [63] S. Brunauer, P. H. Emmett, E. Teller, *J. Am. Chem. Soc.* **1938**, 60, 309.
- [64] E. W. Washburn, *Phys. Rev.* **1921**, 17, 273.